RESEARCH ARTICLE

Key Points:
- Axial Seamount lava flows erupted in 1998, 2011, and 2015 are all transitional MORB, chemically similar to all lavas erupted since 1650 CE
- Lava compositions vary with distance from the caldera consistent with cooling during transport in dikes of 0.5–0.9 °C/km
- The short repose period between 2011 and 2015 resulted in eruption of the hottest lavas at the summit since 1290–1370 CE

Chemical Variations in the 1998, 2011, and 2015 Lava Flows From Axial Seamount, Juan de Fuca Ridge: Cooling During Ascent, Lateral Transport, and Flow

David A. Clague[1] (iD), Jennifer B. Paduan[1] (iD), Brian M. Dreyer[2] (iD), William W. Chadwick Jr[3] (iD), Kenneth R. Rubin[4] (iD), Michael R. Perfit[5] (iD), and Allison T. Fundis[6]

[1]Research Division, Monterey Bay Aquarium Research Institute, Moss Landing, CA, USA, [2]Earth and Planetary Sciences Department, University of California, Santa Cruz, CA, USA, [3]Pacific Marine Environmental Laboratory, NOAA, Hatfield Marine Science Center, Newport, OR, USA, [4]Department of Geology and Geophysics, University of Hawai'i at Mānoa, Honolulu, HI, USA, [5]Department of Geological Sciences, University of Florida, Gainesville, FL, USA, [6]Ocean Exploration Trust, Old Lyme, CT, USA

Abstract Lava flows erupted at Axial Seamount in 1998, 2011, and 2015 are chemically heterogeneous and display decreases in MgO content in their glass rinds with increasing distance from the summit. The trends are consistent with eruption temperature decreases down the rift zones of ~0.5 °C/km within 20 km of the caldera and ~0.9 °C/km at greater distance (only observed in the 2011 eruption). Cooling during magma transport in dikes is the likely cause of the temperature trends observed, related to the effects of cooler wall rocks in areas with less frequent dike intrusions. Flows also cooled as they advanced on the seafloor at rates 3–5 times greater than observed at Kilauea volcano in Hawaii for subaerial tube-fed pahoehoe flows. Lavas erupted in and near the caldera in 1998 and 2011 are slightly enriched transitional mid-ocean ridge basalt that are aphyric and have glass MgO content of 7.1–7.6 wt %. The 2015 lavas have similarly enriched incompatible element compositions typical of transitional mid-ocean ridge basalt, but those erupted inside and on the northeast rim of the caldera contain higher glass MgO of 7.8–8.3 wt % and more abundant plagioclase phenocrysts typical of the normal mid-ocean ridge basaltic lavas erupted between 1290 and 1370 CE. The brief recharge period between the 2011 and 2015 eruptions did not allow magma stored in the shallow reservoir to cool and degas as much as between prior eruptions since 1650 CE, suggesting that the most recent recharge period was shorter than the multicentennial average.

Plain Language Summary Axial Seamount on the Juan de Fuca mid-ocean ridge erupted multiple lava flows of basaltic lava in 1998, 2011, and 2015. The composition of the flows was determined by analysis of 290 lava samples as well as a single sample of volcanic sand produced during mildly explosive eruptive activity in 2015. The lava flows are all hot spot influenced mid-ocean ridge basalt containing few crystals. Basalts cooled at rates of 0.5–1 °C/km and crystallized 15–20% crystals as they were transported away from the summit in dikes. They cooled at rates of ~3 °C/km as they flowed away from the eruptive fissures. Melt composition from the summit region varies in MgO content and temperature. The hottest lavas, at 1201 °C, were those erupted at the summit in 2015 after a 4-year repose period, whereas cooler basalts, at ~1186 °C, erupted at the summit in 2011 after a 13-year repose period. The 1998 lavas had a similar maximum MgO content and temperature to those erupted in 2011 and so may have had a similar repose period, consistent with the average repose period during the last 350 years of eruptive activity. The 2015 summit lavas were the hottest to erupt at Axial Seamount in the last 350 years.

1. Introduction

Globally, mid-ocean ridge (MOR) eruptions are difficult to detect and therefore rarely studied (Perfit & Chadwick, 1998; K. H. Rubin et al., 2012). The Gorda and Juan de Fuca Ridges (JdFR) in the northeastern Pacific have had seven eruptions documented since 1982 due to a combination of water column studies conducted by National Oceanic and Atmospheric Administration (NOAA; e.g., Baker et al., 2012) and the availability, for at least part of the time period, of sound surveillance system (SOSUS) seismoacoustic data that allowed earthquake swarms to be located (e.g., Dziak et al., 2006, 2011) thereby triggering event response cruises (summarized in Cowen et al., 2004). The eruptions in 1986 on the North Cleft segment, 1982–1991 on the CoAxial segment of the JdFR (discovered from seafloor changes between multibeam surveys), 1993 again
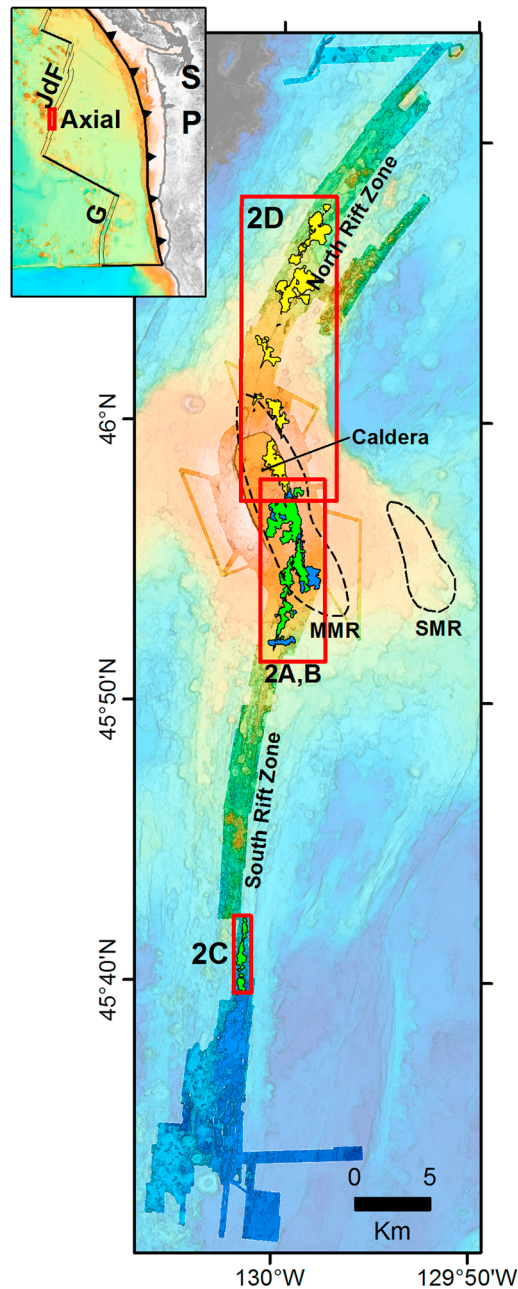
Figure 1. Map with regional location inset showing the location of Axial Seamount on the Juan de Fuca (JdF) mid-ocean ridge offshore the Pacific Northwest. S = Seattle; P = Portland; G = Gorda Ridge. Spreading centers depicted as double light lines, transform faults as single black lines, subduction zones as hachured black line. The main map shows the extent of high-resolution autonomous underwater vehicle mapping data over faded regional ship-based bathymetry. The color ramp extends from orange at 1,375 m depth to dark blue at 2,550 m depth. The summit caldera, north rift zone, and south rift zone are labeled. The dashed line shows the extent of the subcaldera main magma reservoir (MMR) and secondary magma reservoir (SMR) from Arnulf et al. (2014, 2018). The red boxes show the extent of the maps in Figure 2 with Figure 2a showing the 1998 lava flows, Figures 2b and 2c showing the extent of the 2011 lava flows, and Figure 2d showing the extent of the 2015 lava flows. Flows erupted in 1998, 2011, and 2015 are shown in blue, green, and yellow, respectively. Flows erupted in 2011 cover much of those erupted in 1998.

on the CoAxial segment, and 1996 on the north Gorda segment each produced relatively small volume ($<50 \times 10^6$ m^3) elongate hummocky lava flows consisting of pillow mounds (see summary in Yeo et al., 2013, and references therein). The other three known eruptions in the northeast Pacific occurred on Axial Seamount in 1998, 2011, and 2015.

These new lava flows were mapped, sampled, and analyzed to determine the spatial distribution and chemical variations along and away from the eruptive fissures (Caress et al., 2012; W.W. Chadwick et al., 2013, 2016; Clague et al., 2017; Jones et al., 2018). Axial Seamount is not a typical MOR segment because its magma flux and composition are influenced by the Cobb hot spot (J. Chadwick et al., 2005, 2014), but the lavas are mid-ocean ridge basalt (MORB). Many of the eruptive and lava emplacement processes at Axial are more similar to those on MORs than to central volcanoes such as Kilauea, despite the structural similarities of Axial Seamount to Kilauea in having a summit caldera connected to two rift zones. At Axial, the north and south rift zones serve dual functions as the locus of spreading between the Pacific and Juan de Fuca plates and as rift zones where dikes laterally transport magma away from the summit of the seamount.

In the past ~1,000 years, Axial Seamount has erupted two chemical variants of MORB at the summit (Dreyer et al., 2013) that consist of abundant, slightly more incompatible trace-element-enriched Group 1 transitional (T)-MORB and a less enriched Group 2 normal (N)-MORB. These two lava types, besides having different degrees of depletion in incompatible minor and trace elements, also have nonoverlapping ranges in MgO content of the glass (Group 1 lavas contain 7.12–7.73% MgO compared to 7.84–8.72% MgO for Group 2), abundance of phenocrysts (Group 1 are generally aphyric, whereas Group 2 tend to be plagioclase phyric to ultraphyric), and age (Group 1 caldera lavas are younger than 365 years old, and Group 2 caldera and near-caldera lavas are between 650 and 730 years old) (Dreyer et al., 2013). In this paper, the major and trace element chemistry of the three historical flows will be used to evaluate why the 2015 eruption differs from prior Group 1 eruptions and why the lava compositions from each eruption vary downrift along the eruptive fissures.

2. Geological Setting

Axial Seamount is a submarine volcano located in the northeast Pacific at the intersection of the Cobb hot spot chain (J. Chadwick et al., 2005, 2014; Desonie & Duncan, 1990; Johnson & Embley, 1990; Rhodes et al., 1990) and the JdFR (Figure 1). The seamount rises to a depth of 1,367 m and has a horseshoe-shaped 3 × 8 km summit caldera, deeper to the north end, and north and south rift zones that each extend more than 50 km from the summit (Embley et al., 1990). The north rift zone intersects the caldera near the center of the north wall of the caldera. Fissures associated with the north rift also extend along the western caldera floor and outside the caldera in the upper western flank. The south rift zone intersects the SE corner of the caldera, and numerous fissures extend across the eastern caldera floor and in the east upper flank. The summit region is underlain by two magma reservoirs with the main reservoir up to a kilometer thick, roughly twice the size of the caldera and whose upper surface is between 1.1 and 2.8 km below the seafloor (Arnulf et al., 2014, 2018; West et al., 2001). The second reservoir is located ~10 km to the SSE of Axial's summit caldera. The two magma reservoirs contain between 26 and 60 km^3 of melt (Arnulf et al., 2018).
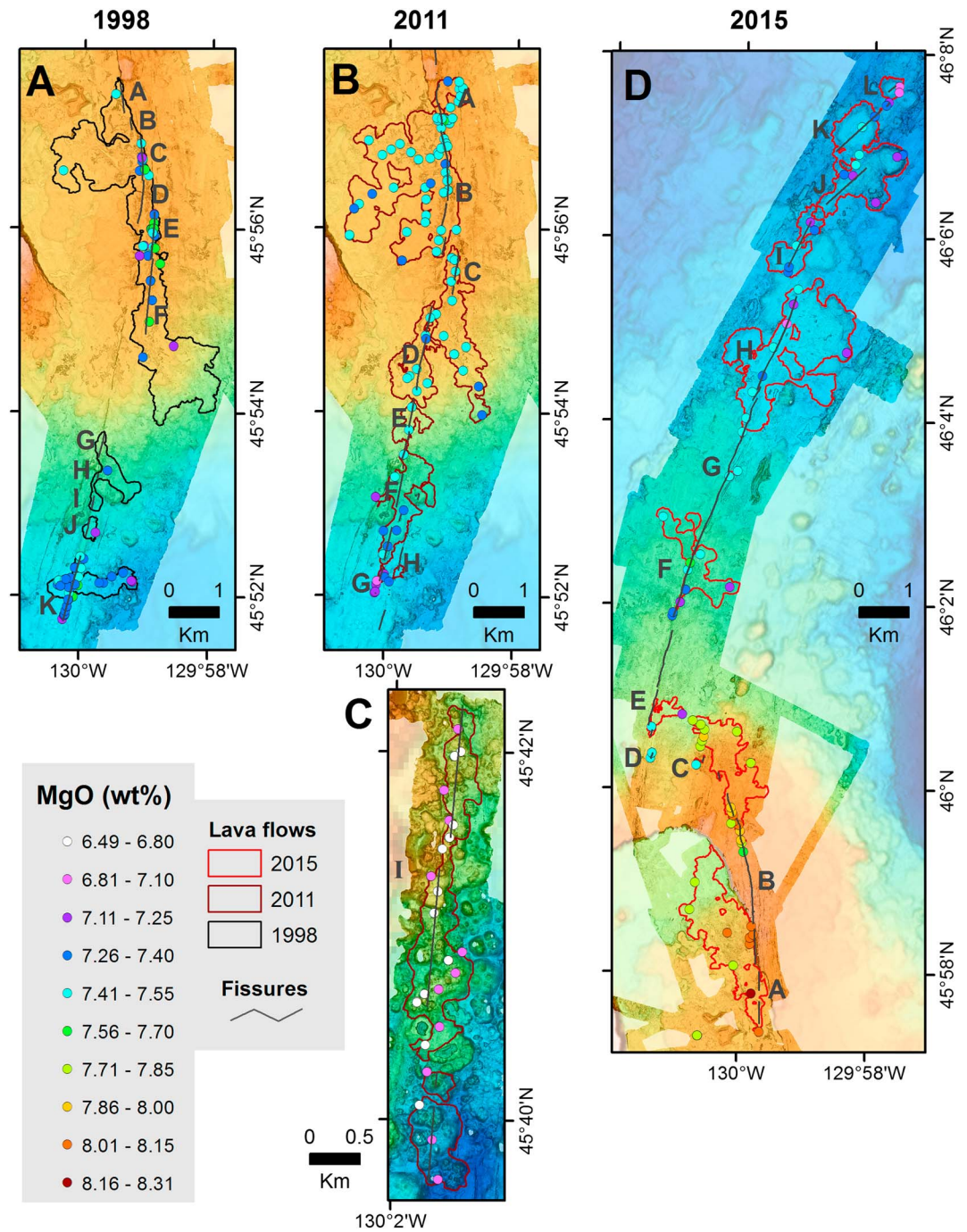
Figure 2. Autonomous underwater vehicle high-resolution bathymetric maps of portions of Axial Seamount from Clague et al. (2017) showing lava flow boundaries, locations of eruptive fissures (labeled alphabetically from A nearest the summit) and the locations of lava samples, color-coded for MgO content of the glasses as in the figure legend. (a) 1998 lava flows at the summit and upper south rift. Fissures as defined in W. W. Chadwick et al. (2013). (b) Proximal 2011 lava flows in and near the caldera and upper south rift. (c) Distal 2011 lava flows on the deep south rift. (d) The 2015 lava flows in the caldera, on the northeast rim of the caldera, and along the north rift. Color ramp is 1,390 to 2,300 m depth in a, b, and d and 1,800–2,350 in c.

The three historical eruptions in 1998, 2011, and 2015 are the most recent of at least 50 mapped lava flows erupted in the last 1,600 years (Clague et al., 2013). All three were mapped at 1-m resolution using multibeam sonars mounted on autonomous underwater vehicles (AUV). The flow extents used here (Figure 2, Clague

Table 1
Key Chemical Characteristics of Axial Seamount Historical Flows With Additional Prehistorical Flow Averages

Flow unit	Samples	MgO Maximum	MgO Minimum	MgO average	K_2O/TiO_2	Zr/Y	Zr/Nb	$(La/Sm)_{C1}$	$(La/Yb)_{C1}$	Age
2015 A	7	8.31	8.03	8.06 ± 0.19	0.118 ± 0.004	3.13	18.9	0.89	1.14	3 years
2015 Pyroaphyric	10	8.16	7.93	8.08 ± 0.07	0.120 ± 0.007					
2015 B	9	8.03	7.83	7.93 ± 0.08	0.121 ± 0.006	3.13	19.0	0.90	1.14	
2015 Pyromicrolites	9	7.97	7.59	7.74 ± 0.13	0.119 ± 0.009					
2015 C	1			7.50	0.112					
2015 D–G	17	7.66	7.23	7.43 ± 0.10	0.116 ± 0.004					
2015 H	7	7.54	7.09	7.33 ± 0.17	0.111 ± 0.004					
2014 I	4	7.41	7.10	7.31 ± 0.14	0.112 ± 0.006					
2015 J	6	7.44	7.11	7.34 ± 0.13	0.115 ± 0.003					
2015 K	4	7.34	7.05	7.17 ± 0.13	0.118 ± 0.007					
2015 all	54	8.31	7.05	7.56 ± 0.31	0.116 ± 0.005	3.11	19.5	0.87	1.12	
2011 A–D	53	7.54	7.25	7.45 ± 0.06	0.112 ± 0.005					7 years
2011 E–F	10	7.48	7.25	7.39 ± 0.08	0.112 ± 0.005					
2011 G–H	7	7.32	7.10	7.21 ± 0.07	0.113 ± 0.005					
2011 A–H	70	7.54	7.10	7.42 ± 0.10	0.112 ± 0.005	3.05	20.9	0.82	1.05	
2011 I	29	6.93	6.49	6.73 ± 0.12	0.114 ± 0.004	3.12	19.9	0.85	1.10	
1998 A–J	46	7.64	7.11	7.39 ± 0.14	0.120 ± 0.007					20 years
1998 K	34	7.65	7.11	7.41 ± 0.09	0.108 ± 0.007					
1998 all	80	7.65	7.11	7.40 ± 0.12	0.115 ± 0.009	3.2	20.4	0.87	1.11	
Postcaldera Group 1	69	7.73	7.12	7.47 ± 0.14	0.108 ± 0.006	3.07	20.1	0.86	1.09	<365 years
Ne	11	7.92	7.64	7.82 ± 0.10	0.119 ± 0.003	3.28	20.5	0.97	1.08	365 years
Group 2-Eg	9	8.38	8.17	8.30 ± 0.06	0.088 ± 0.004	2.82	24.5	0.74	0.83	685 years
Group 2-all	60	8.72	7.84	8.34 ± 0.20	0.089 ± 0.008	2.82	25.4	0.73	0.90	650–730 yrs
Precaldera Group 1	53/32	7.71	7.26	7.52 ± 0.13	0.112 ± 0.005	3.05 ± 0.07	20.2 ± 1.2	0.86 ± 0.05	1.02 ± 0.06	>~1,200 years

et al., 2017), are modified from W. W. Chadwick et al. (2013) for 1998 flows, from Caress et al. (2012) for 2011 flows, and from W. W. Chadwick et al. (2016) for 2015 flows based on more complete AUV high-resolution mapping. The morphology, eruptive fissure length, areal coverage, maximum and average flow thicknesses, and volumes of the flows are summarized in Table 1 in Clague et al. (2017), and the eruption chronologies are summarized in Clague et al. (2017) and Wilcock et al. (2018, and references therein). The lava flows increased in area covered from 1998 to 2011 to 2015 from 7.1×10^6 to 10.2×10^6 to 11.5×10^6 m^2 and in volume from 24×10^6 to 94×10^6 to 155×10^6 m^3 (Clague et al., 2017).

Some chemical characteristics of lavas erupted at Axial Seamount over the last 1,000–1,200 years are outlined in Table 1. The precaldera flows exposed in the caldera walls and as seafloor surface flows surrounding the caldera are almost all aphyric Group 1 lavas (Dreyer et al., 2013) and are compositionally indistinguishable from the Group 1 lavas erupted after 1650 CE. After the present caldera formed, sometime between 750 and 950 CE (i.e., as determined from the minimum ages rather than maximum ages as incorrectly used in Clague et al., 2013) of sediment cores on the caldera rims, Group 2 lavas erupted inside the caldera and on the east flank (flow Eg of Clague et al., 2013) at least from 1290 to 1370 CE (Clague et al., 2013). A single flow designated Ne erupted inside the northeastern to north central caldera ~1650 CE (Clague et al., 2013); it has a slightly more enriched composition than other Group 1 lavas (Dreyer et al., 2013; Table 1). The change from Group 2 to Group 1 lavas is not synchronous with caldera formation, which occurred between 1,000 and 1,300 years ago. Instead, it occurred at least 700 years later.

The 1998 and 2011 flows erupted at the southeastern part of the caldera and along the south rift, whereas the 2015 flows erupted at the summit inside the northeastern caldera, on the northeast rim of the caldera, and along the north rift (Figure 2). Lava flows from all three eruptions are thin channelized flows near the summit and upper rift zones that transition to much thicker and more voluminous hummocky flows farther down the rift zones (see summary in Clague et al., 2017).

The lava flows produced during the three historical eruptions are extensively sampled with 95 samples of the 1998 flows, 122 of the 2011 flows, and 73 of the 2015 flows plus a sample of pyroclastic glass shards. In comparison, the next most extensively sampled flows on the global MOR system are characterized by fewer

Table 2
Average Major Element Microprobe Compositions of Glasses, Separated by Laboratory Where the Samples Were Analyzed and Eruptive Fissures as Shown in Figure 2

Flow unit	Lab	S	Cl	Total	SiO_2	TiO_2	Al_2O_3	FeO	MnO	MgO	CaO	Na_2O	K_2O	P_2O_5	K_2O/TiO_2	HI
1998 (47)[a]	USGSD	na	na	99.06	50.23	1.53	14.55	10.71	0.20	7.38	12.16	2.91	0.19	0.15	0.123	1.22
2σ		na	na	0.92	0.38	0.04	0.18	0.28	0.02	0.32	0.30	0.16	0.02	0.02	0.008	
1998 (35)[b]	USGSM	0.124	0.021	100.15	49.89	1.55	14.65	11.01	0.19	7.39	12.29	2.72	0.17	0.14	0.108	0.98
2σ		0.017	0.008	0.64	0.34	0.08	0.14	0.31	0.02	0.17	0.16	0.11	0.02	0.02	0.011	
1998 (13)[b]	UCD	0.127	0.024	100.37	49.77	1.55	14.62	11.06	0.20	7.41	12.33	2.74	0.17	0.15	0.112	0.92
2σ		0.026	0.006	0.74	0.30	0.06	0.18	0.28	0.02	0.28	0.16	0.06	0.02	0.02	0.008	
2011 (76) A–E	UCD	0.142	0.023	100.56	49.84	1.53	14.62	11.03	0.19	7.45	12.29	2.73	0.17	0.14	0.112	0.68
2σ		0.014	0.010	0.64	0.16	0.04	0.16	0.14	0.02	0.11	0.16	0.05	0.01	0.02	0.008	
2011 (15) F–H	UCD	0.146	0.021	100.63	49.76	1.60	14.60	11.28	0.19	7.26	12.19	2.79	0.18	0.14	0.111	1.30
2σ		0.016	0.010	0.84	0.28	0.12	0.26	0.46	0.02	0.32	0.16	0.10	0.02	0.04	0.008	
2011 (29) I	UCD	0.157	0.026	100.44	49.84	1.77	14.15	12.18	0.20	6.73	11.86	2.90	0.20	0.17	0.114	1.08
2σ		0.014	0.008	0.50	0.22	0.10	0.32	0.56	0.02	0.24	0.24	0.04	0.02	0.02	0.008	
2015 (10) A	UCD	0.136	0.019	100.88	49.28	1.42	15.42	10.54	0.18	8.02	12.25	2.61	0.16	0.11	0.116	1.20
2σ		0.012	0.014	0.62	0.42	0.08	0.22	0.26	0.02	0.40	0.16	0.06	0.01	0.06	0.010	
2015 (10) aphyric[c]	UCD	0.135	0.020	101.18	49.41	1.44	15.32	10.40	0.19	8.08	12.22	2.64	0.17	0.14	0.120	1.27
2σ		0.020	0.018	0.76	0.34	0.12	0.14	0.16	0.06	0.14	0.12	0.06	0.04	0.06	0.014	
2015 (19) B–C	UCD	0.137	0.023	100.74	49.30	1.46	15.36	10.69	0.19	7.83	12.23	2.66	0.17	0.12	0.118	1.46
2σ		0.016	0.022	0.88	0.70	0.08	0.48	0.32	0.04	0.28	0.24	0.08	0.02	0.04	0.012	
2015 (9) microphyric[c]	UCD	0.134	0.030	100.92	49.59	1.46	15.33	10.47	0.18	7.74	12.26	2.66	0.17	0.13	0.119	1.16
2σ		0.014	0.024	0.52	0.28	0.08	0.44	0.34	0.04	0.26	0.16	0.02	0.02	0.04	0.018	
2015 (16) D–F	UCD	0.142	0.033	99.75	49.96	1.56	14.73	10.89	0.20	7.41	12.09	2.81	0.18	0.16	0.116	1.17
2σ		0.012	0.026	1.84	0.30	0.08	0.24	0.44	0.02	0.24	0.20	0.08	0.02	0.04	0.010	
2015 (19) G–J	UCD	0.146	0.023	100.49	49.86	1.60	14.57	11.20	0.20	7.30	12.14	2.80	0.18	0.16	0.114	1.22
2σ		0.014	0.006	0.98	0.22	0.10	0.26	0.48	0.02	0.28	0.22	0.08	0.02	0.04	0.010	
std.VG2 (32)	UCD	0.154	0.030	100.12	50.71	1.86	14.10	11.86	0.21	7.11	11.16	2.60	0.20	0.20	0.106	
2σ		0.027	0.014	0.98	0.38	0.08	0.17	0.34	0.04	0.22	0.28	0.04	0.02	0.02	0.020	

Note. Analyses of S, Cl, and Totals are as determined with other oxides normalized to 100% on a volatile-free basis. Full data set is in Table S1. USGSD = U.S. Geological Survey Denver; USGSM = U.S. Geological Survey Menlo Park; UCD = University of California at Davis; HI = homogeneity index. Number in parentheses is number of samples averaged.
[a]From J. Chadwick et al. (2005).   [b]From Clague et al. (2013).   [c]Pyroclasts from W. W. Chadwick et al. (2016).

samples, with the 2005–2006 lava flows at ~9°50′N on the East Pacific Rise (EPR) characterized by 58 dive samples (Goss et al., 2010), the Animal Farm flows at 18°35′S on the EPR by 53 samples (Sinton et al., 2002), and the Aldo Kihi flows at 17°30′S by 51 samples (Bergmanis et al., 2007). Here we summarize the variations in compositions of the Axial flows produced by the three eruptions, both along their eruptive fissures and away from the fissures, to evaluate cooling rates during (1) transport in the dikes feeding the eruptions and (2) as channelized lava flows advanced on the seafloor, as well as how the historical lava flows fit into the recently proposed longer/intermediate-term geochemical evolution at Axial Seamount.

3. Methods

Forty-seven of the 95 samples of 1998 lava (supporting information Table S1) were analyzed by electron microprobe at the U.S. Geological Survey (USGS) in Denver (J. Chadwick et al., 2005), 35 at the USGS in Menlo Park (Clague et al., 2013), and 13 at the University of California at Davis (UC Davis; all but two in Clague et al., 2013). The 2011 and 2015 (Table S1) lava samples were all analyzed at the UC Davis. Fifty analyses of 117 samples of 2011 lavas from the caldera and upper south rift are published in Jones et al. (2018), whereas 30 analyses of the 2015 lavas and 19 of pyroclasts are published in W. W. Chadwick et al. (2016). Analyses from the three eruptions published here for the first time total 117, and average analyses are presented in Table 2. The samples analyzed at USGS in Menlo Park and at UC Davis used similar methodology, with the Smithsonian glass standard VG2 used as the primary standard for the major oxides SiO_2, Al_2O_3, FeO, MgO, CaO, and Na_2O, and rutile for TiO_2, synthetic Mn-oxide or rhodonite for MnO, potassium feldspar for K_2O, apatite for P_2O_5, troilite or pyrrhotite for S, and scapolite or sodalite for Cl. Off-peak backgrounds bracketed the element peak and five spot analyses done on different glass grains using a ~5-μm defocused beam were averaged. The MgO concentration in VG2 was adjusted from the reported 6.71 (Jarosewich et al., 1980) to 7.07 wt % based on

Table 3
Average ICP Trace Element Analyses for Axial Seamount Historical Flows Subdivided by Eruptive Fissures as Shown in Figure 2

Flow unit	Sc	V	Cr	Co	Ni	Rb	Sr	Y	Zr	Nb	Cs	Ba	La	Ce	Pr	Nd
Ne	48.5	278.9	315.3	40.5	53.7	2.27	166.3	30.4	99.6	4.86	0.014	28.4	4.93	13.03	2.05	10.86
1σ (2)	0.1	3.9	2.2	0.6	0.1	0.14	0.4	0.2	0.6	0.15	0.003	0.6	0.07	0.05	0.01	0.43
1998-UC laser	48.7	306.5	279.7	39.7	45.1	2.19	152.7	30.5	94.0	4.61	0.018	27.6	4.69	12.81	2.01	10.35
1σ (4)	0.3	2.5	8.7	0.2	1.0	0.10	1.1	0.7	2.3	0.05	0.004	0.3	0.07	0.09	0.03	0.31
1998 UC solution	47.9	321.8	279.7	48.4	50.6	2.36	152.2	32.5	100.2	4.92	0.024	27.8	4.75	12.68	2.04	10.75
1σ (3)	0.5	3.7	2.3	0.3	0.5	0.01	1.6	0.3	0.6	0.06	0.004	0.4	0.07	0.20	0.03	0.05
1998-Chadwick	62.0	292.1	273.1		46.3	2.23	150.7	29.9	98.3	4.76			4.84	13.38	2.13	11.16
1σ (8)	2.4	5.1	31.0		3.7	0.39	3.7	0.8	1.6	0.41			0.15	0.22	0.05	0.26
2011A–H	48.9	301.3	268.8	44.5	45.6	2.12	155.8	31.0	94.7	4.56		27.6	4.68	12.82	2.04	10.73
1σ (13)	1.3	8.5	26.0	3.3	3.3	0.20	2.5	1.1	3.5	0.13		0.8	0.16	0.34	0.05	0.39
2011I	47.3	334.6	95.1	47.1	35.3	2.35	157.8	35.3	110.0	5.52		31.0	5.39	14.87	2.34	12.23
1σ (5)	0.9	6.7	29.6	0.6	8.0	0.02	1.8	1.0	4.4	0.24		1.0	0.21	0.60	0.13	0.45
2015A	44.7	290.9	301.2	48.8	59.1	2.07	157.1	28.0	87.8	4.65	0.021	26.7	4.43	11.80	1.88	9.79
1σ (4)	1.4	10.0	19.1	1.1	2.3	0.06	3.0	1.1	3.3	0.17	0.000	0.6	0.14	0.37	0.06	0.34
2015B	45.2	295.9	315.3	49.3	59.0	2.10	157.1	28.2	88.2	4.67	0.022	26.9	4.50	11.92	1.90	9.90
1σ (2)	0.6	3.1	6.4	0.9	1.5	0.06	5.0	0.5	1.5	0.05	0.001	0.8	0.14	0.38	0.05	0.27
2015E–J	47.9	319.5	274.6	47.8	46.4	2.18	153.8	31.5	97.6	4.92	0.022	27.6	4.79	12.92	2.07	10.85
1σ (8)	1.5	7.7	20.8	1.3	1.9	0.11	3.5	1.2	5.8	0.30	0.001	1.1	0.28	0.67	0.10	0.51

Note. Full data set is in Table S2. Number in parentheses indicates number of samples averaged and used to calculate 1 sigma uncertainty. ICP = inductively coupled plasma.

recalibration against Smithsonian glass standards A99 and 113716; fused rock standards BHVO-2, BCR-2, and BIR; and EPR MORB glass Alvin 2392–9. This MgO value is even higher than 6.95 wt % recently reported by Helz et al. (2014) but is consistent with the value for widely used MORB glass Alvin 2392-9. Methods for the analyses at USGS in Denver were previously reported in Appendix A of J. Chadwick et al. (2005).

J. Chadwick et al. (2005) report solution inductively coupled plasma-mass spectrometry (ICP-MS) trace element analyses of eight 1998 samples using techniques described therein. ICP-MS trace element analyses at the University of California at Santa Cruz were done for four additional samples from the 1998 flows (Dreyer et al., 2013), although we note that sample T874-R8 was incorrectly identified as 1998 lava; it is actually from a flow underlying the 1998 flows. Three 1998 lavas were analyzed using solution ICP-MS, and the same samples, with one additional sample, were analyzed using laser ablation ICP-MS techniques, instrument settings, and with precision and accuracy described in Dreyer et al. (2013) and standard analyses repeated in Table S2. The same laser ablation ICP-MS techniques were used to analyze 17 new samples from the 2011 flows, and the same solution ICP-MS techniques were used to analyze 14 from the 2015 flows (Table S2 with average analyses in Table 3).

The evaluation of chemical variations in the three flows as a function of distance traveled required quantification along the fissure system. Each sample location was projected onto the nearest point on the appropriate eruptive fissure (for lavas that simply flowed away from the fissure) in a Geographic Information System or onto the nearest point along a channel, then backtracked along the channel to the point on the fissure where the channel began. The distances from the uppermost part of the fissure system to these projected points are in Table S1. The distance traveled on the surface for fissure-erupted lavas is the distance from the projected point along the fissure to the sample location, and for samples that flowed down a channel, it is the distance along the route of the channel from the fissure to the projected point, plus the distance from the projected point to the collection location. The measured distances are slightly larger (perhaps a few percent) than if an average single dike had been used for the projections.

4. Results

The chemistry of lavas from the three eruptions are described in chronological sequence as the 1998 and 2011 lavas are nearly identical to those erupted since 1650 CE, and the 2015 flows are chemically and mineralogically distinctive. All three flows follow typical low-pressure liquid lines of descent with increasing FeO,

Table 3 *(continued)*

Flow unit	Sm	Eu	Gd	Tb	Dy	Ho	Er	Tm	Yb	Lu	Hf	Ta	Pb	Th	U
Ne	3.18	1.22	4.59	0.805	5.28	1.12	3.35	0.474	3.16	0.441	2.59	0.309	0.497	0.332	0.109
1σ (2)	0.00	0.02	0.02	0.015	0.11	0.04	0.10	0.043	0.15	0.014	0.09	0.031	0.045	0.005	0.002
1998-UC laser	3.37	1.28	4.56	0.777	5.16	1.08	3.21	0.469	3.02	0.458	2.39	0.283	0.489	0.307	0.103
1σ (4)	0.10	0.05	0.18	0.010	0.20	0.03	0.06	0.014	0.12	0.010	0.10	0.017	0.023	0.007	0.002
1998 UC solution	3.37	1.28	4.47	0.811	5.12	1.11	3.15	0.477	3.03	0.445	2.52	0.298	0.473	0.301	0.107
1σ (3)	0.09	0.01	0.06	0.002	0.11	0.02	0.05	0.011	0.02	0.002	0.02	0.001	0.008	0.001	0.001
1998-Chadwick	3.58	1.39	4.75	0.863	5.30	1.15	3.03	0.500	3.11	0.500		0.324			
1σ (8)	0.18	0.04	0.09	0.052	0.14	0.05	0.12	0.000	0.14	0.000		0.014			
2011A–H	3.58	1.29	4.68	0.805	5.27	1.16	3.31	0.494	3.21	0.463	2.43	0.289	0.483	0.309	0.101
1σ (13)	0.15	0.05	0.26	0.045	0.27	0.08	0.13	0.033	0.15	0.038	0.09	0.013	0.052	0.012	0.006
2011I	3.96	1.48	5.15	0.920	6.11	1.32	3.96	0.565	3.54	0.575	2.80	0.342	0.496	0.360	0.115
1σ (5)	0.25	0.05	0.20	0.056	0.17	0.02	0.32	0.030	0.32	0.028	0.23	0.019	0.010	0.017	0.005
2015A	3.11	1.20	4.17	0.738	4.80	1.02	2.91	0.431	2.71	0.411	2.33	0.300	0.449	0.287	0.102
1σ (4)	0.10	0.04	0.16	0.030	0.19	0.04	0.10	0.019	0.12	0.015	0.09	0.010	0.013	0.009	0.004
2015B	3.11	1.23	4.20	0.755	4.84	1.03	2.96	0.442	2.75	0.415	2.37	0.303	0.452	0.291	0.105
1σ (2)	0.06	0.03	0.08	0.008	0.04	0.01	0.04	0.008	0.05	0.006	0.03	0.003	0.010	0.008	0.002
2015E–J	3.47	1.31	4.65	0.826	5.34	1.15	3.28	0.487	3.06	0.464	2.60	0.324	0.478	0.312	0.112
1σ (8)	0.14	0.05	0.18	0.031	0.20	0.04	0.12	0.018	0.13	0.018	0.14	0.016	0.018	0.029	0.014

TiO_2, K_2O, P_2O_5, Na_2O, S, and incompatible trace elements with decreasing MgO, Al_2O_3, and compatible trace elements (e.g., Langmuir et al., 1992; Perfit & Chadwick, 1998). Dreyer et al. (2013) described and discussed the origin of major and trace element variations and modeled low-pressure crystal fractionation for Axial compositions. The historical lavas fall well within the range of compositions considered in that study, and the reader is referred there for more details. For the remainder of the paper, we have used MgO content of the glass as a proxy for extent of fractionation. In addition, the quench temperature (the temperature at which melt is quenched in seawater to glass) can be calculated using $T°C = 19.044*MgO + 1042.85$ with MgO in weight percent (Sugawara, 2000, with MgO converted from mole percent to weight percent and T from degrees Kelvin (°K) to Celsius (°C)), which allows us to evaluate cooling during magma transport through dikes or on the surface during flow emplacement. Relative temperatures are as precise as the MgO analyses by electron microprobe, or $2\sigma = 4$ °C, based on repeat analyses of standard VG2 (Table 2).

Homogeneity index (HI) is the average of the ratio of the two standard deviations (2σ) from the mean for each element divided by the 2σ analytical uncertainty for that element (Rhodes, 1983) and gives a measure of compositional variability relative to analytical uncertainty. Higher HI values indicate less homogeneity. The HI values reported here are based on the major and minor element compositions, not including S and Cl, determined by electron microprobe.

4.1. The 1998 Eruption

In 1998, four discrete channelized flows were produced from 11 identified en echelon fissures extending a distance of 11 km in the southeastern caldera floor and the upper south rift zone (W. W. Chadwick et al., 2013). Flows from fissures 98A to 98F and 98G to 98I coalesced into single composite flows (Figure 2a).

Dives in 2016 to sample 2015 flows along the upper north rift had a difficult time identifying the new flows in places due to locally abundant orange-brown sediment/bacterial mat that was deposited on both new and adjacent older flows. The 1998 and 2011 flows inside the caldera also were locally covered with similar hydrothermal deposits a few months after the eruptions. Two samples (R501-4 and R501-6; J. Chadwick et al., 2005) collected following the 1998 eruption were misidentified (see Clague et al., 2013) as 1998 lavas. Two other samples (J2-581-pillow 2 and J2-581-pillow 30, Table S1) were collected as 2011 lavas but based on Po analysis (K. R. Rubin, unpublished data, December 2017) have been assigned to the adjacent 1998 flow.

The aphyric to sparsely plagioclase-phyric 1998 flows vary from 7.11 to 7.66 wt % MgO along the 11 km of eruptive fissures (Table 2 and Figures 2a and 3a). Average compositions for lavas sampled near eruptive fissures 98A to 98K (W. W. Chadwick et al., 2013) and labeled as A to K in Figure 2a contain between 7.38 and 7.43 wt % MgO for analyses done on three different microprobes and within analytical uncertainty of each
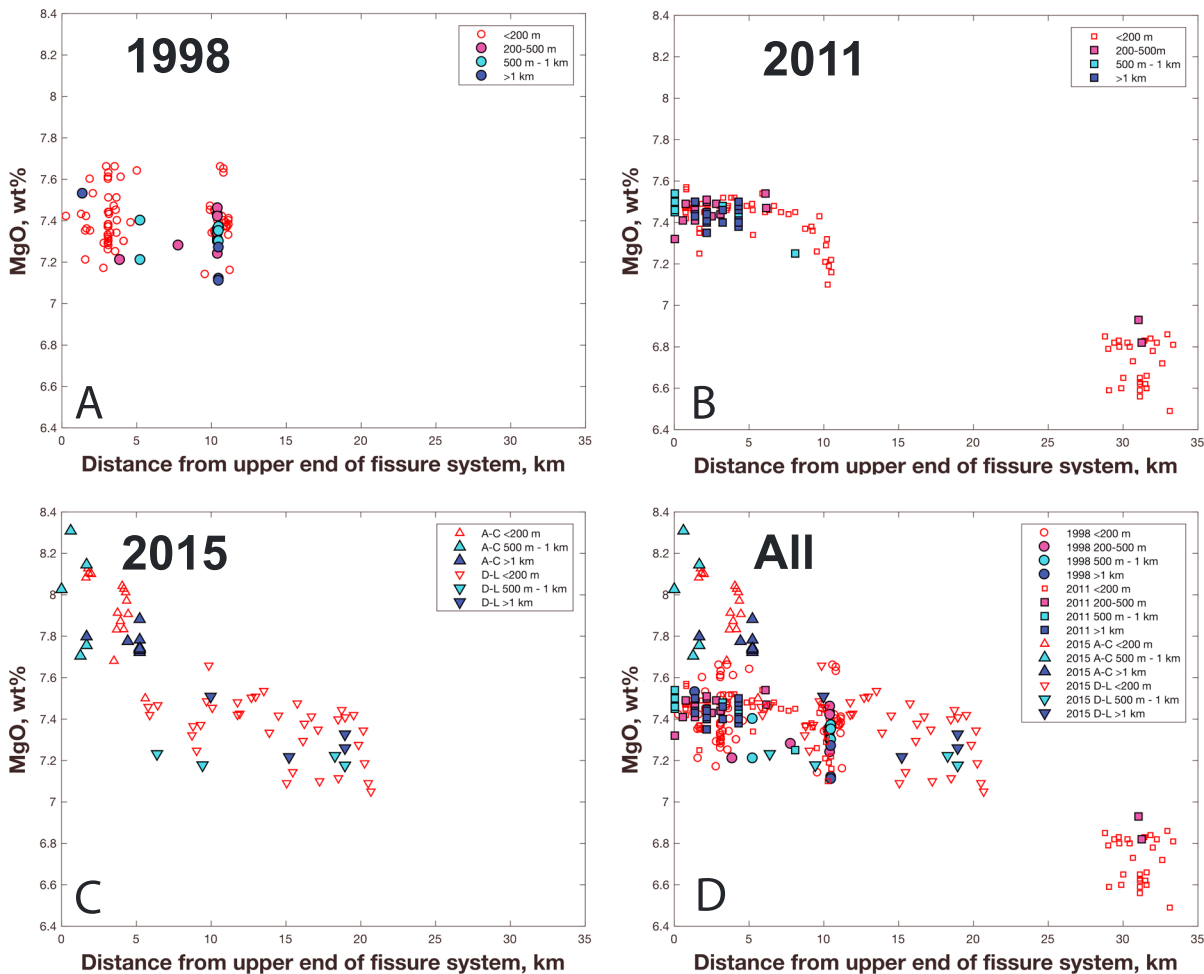
Figure 3. Plots of MgO content of normalized microprobe glass analyses as a function of distance (measured as described in the text and listed in Table S1) along the fissures from the uppermost end of the eruptive fissures. All four panels have the same scales in distance and in MgO content in weight percent (wt %). The samples are subdivided into four groups (symbols in legend) for each eruption depending on the distance the flow traveled on the surface (measured as described in the text and listed in Table S1). The near-fissure samples traveled <200 m from the fissures, the next closest 200–500 m from the fissures, the next group 500 m to 1 km from the fissures, and the final group traveled >1 km from the fissure. (a) The 1998 lava flows. (b) The 2011 lava flows. (c) The 2015 lava flows. (d) All three historial flows.

other (e.g., analytical accuracy and 2σ precision for all elements are listed in Table S1). Samples and thus data are sparse, but lavas near fissures 98G-H (flows coalesced into single flow) and 98J have lower MgO (7.28 and 7.14 wt % MgO), compared to the lavas erupted at the summit. The 11 analyses done at UC Davis (Table S1) show a decrease in MgO from ~7.6 wt % a few kilometers from the north end of the fissure system to ~7.3 wt % about 10 km to the south. The average of all samples is 7.39 ± 0.26 (2σ) wt % MgO. Few samples were collected at the distal ends of flows, except for the southernmost flow where distal samples are indistinguishable from upslope near-fissure samples (Figure 2a). The samples are all Group 1 T-MORB, using the criteria for Axial T-MORB of $K_2O/TiO_2 > 0.10$ (Dreyer et al., 2013), with $K_2O/TiO_2 = 0.115 ± 0.009$. Their trace element compositions are consistent with T-MORB with Zr/Nb ~ 20 and Zr/Y ~ 3.2, and only slight middle rare earth element enrichments in primitive mantle-normalized patterns (Figure 4) and with $(La/Sm)_{C1}$ ~ 0.87 and $(La/Yb)_{C1}$ ~ 1.11, similar to the average of prehistorical Group 1 lavas (Table 1).

All lava flows cover surfaces consisting of prior lava flows. Based on stratigraphic relations revealed in the bathymetric maps, the 1998 flows in the caldera partly covered parts of six different flows (Clague et al., 2013), whereas those on the upper south rift partly covered parts of four flows and three cones.
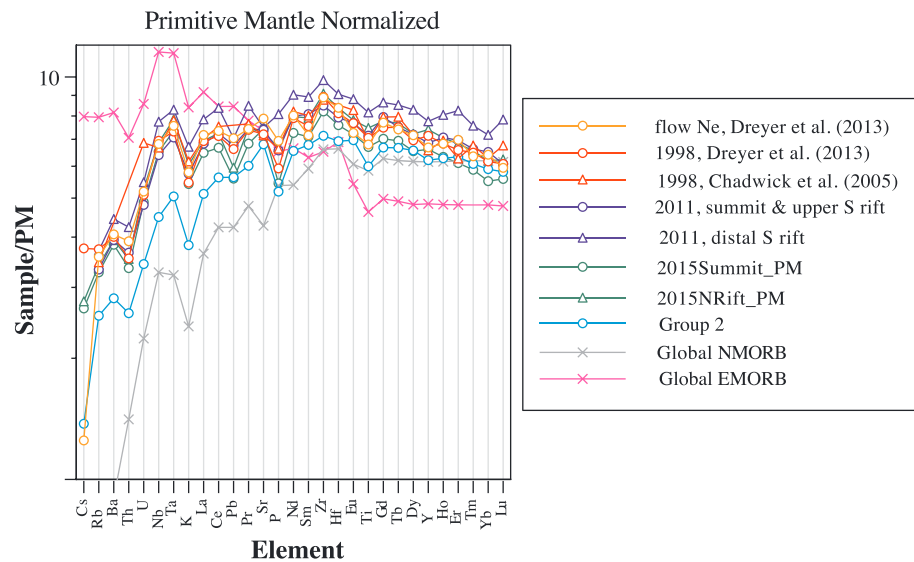
Figure 4. Primitive mantle normalized spidergram for historical flows or portions of flows from Axial Seamount, an average prehistorical Group 2 N-MORB (Dreyer et al., 2013), and 365-year-old flow Ne (Clague et al., 2013), the oldest dated post-Group 2 lava that erupted from a fissure system extending N-S in the eastern caldera. Also shown are global average N-MORB and E-MORB from O'Neill and Jenner (2012). Primitive mantle values are from Sun and McDonough (1989). None of the Axial lavas are chemically similar to global E-MORB or even to global N-MORB, although Axial Group 2 lavas are almost as depleted as global N-MORB. Lavas from all three historical lavas are similar to Group 1 lavas and only slightly more depleted than flow Ne. The average 2015 summit lava has the lowest concentrations, and the distal south rift 2011 lavas have the highest concentrations of incompatible elements and so are inversley correlated with MgO content of the glasses. N-MORB = normal mid-oceanic ridge basalt; E-MORB = enriched mid-ocean ridge basalt.

4.2. The 2011 Eruption

In 2011, 12 discrete flows erupted from eight en echelon sometimes discontinuous fissures on the southeastern rim of the caldera, on the caldera floor, and on the upper south rift (Figure 2b), with one more fissure on the lower south rift (Caress et al., 2012; Clague et al., 2017; Figure 2c). The flows on the southeast caldera rim, caldera floor, and most of the upper south rift are channelized flows, but the southernmost flows on the upper south rift are hummocky flows as are the three flows erupted from a single fissure on the deep south rift. The fissures are labeled A to H (Figure 2b) and referred to as 11A to 11H in the text, with 11A the northernmost in the summit caldera and 11H the southernmost on the upper south rift. These lavas are aphyric with only rare plagioclase phenocrysts. The summit and upper south rift lavas range from 7.07 to 7.57 wt % MgO (Table 2 and Figure 3b).

The average lavas erupted from fissures 11A-D, 11E-F, and 11G-H have 7.45 ± 0.12 (2σ), 7.39 ± 0.16, and 7.21 ± 0.14 wt % MgO, respectively, suggesting a small decrease in MgO away from the summit (Figure 2b). The average of all 2011 summit and upper south rift samples is 7.42 ± 0.20 wt % MgO, which is statistically the same as for the 1998 flows (see Table 2). Samples from distal ends and mid-distance of flow lobes inside the caldera and to the southeast are not significantly more evolved than near-fissure samples (Figure 2b and 3b).

Three discrete hummocky flows on the lower south rift zone erupted from fissure 11I (Figure 2c). They erupted from a 4.8-km-long fissure separated from the upper rift fissures by about 20.6 km. These lavas are significantly more differentiated (Table S2 and Figure 2c) and range from 6.49 to 6.94 wt % MgO, with an average of 6.73 ± 0.12 wt % MgO (Figure 3b) and a random spatial variation. They contain abundant microlites of plagioclase, clinopyroxene, and olivine. Minor overlap of the electron beam on microlites may account for some of the variation observed in the microprobe glass compositions.

The upper rift and caldera lavas (erupted from fissures 11A to 11H) are Group 1 T-MORB with K_2O/TiO_2 = 0.112 ± 0.005, Zr/Nb ~ 3.05, Zr/Y ~ 21, $(La/Sm)_{C1}$ ~ 0.82, and $(La/Yb)_{C1}$ ~ 1.05 (Table 1). The distal south rift (fissure 11I) lavas are also Group 1 T-MORB with K_2O/TiO_2 = 0.114 ± 0.004, Zr/Nb ~ 3.12, Zr/Y ~ 20, $(La/Sm)_{C1}$
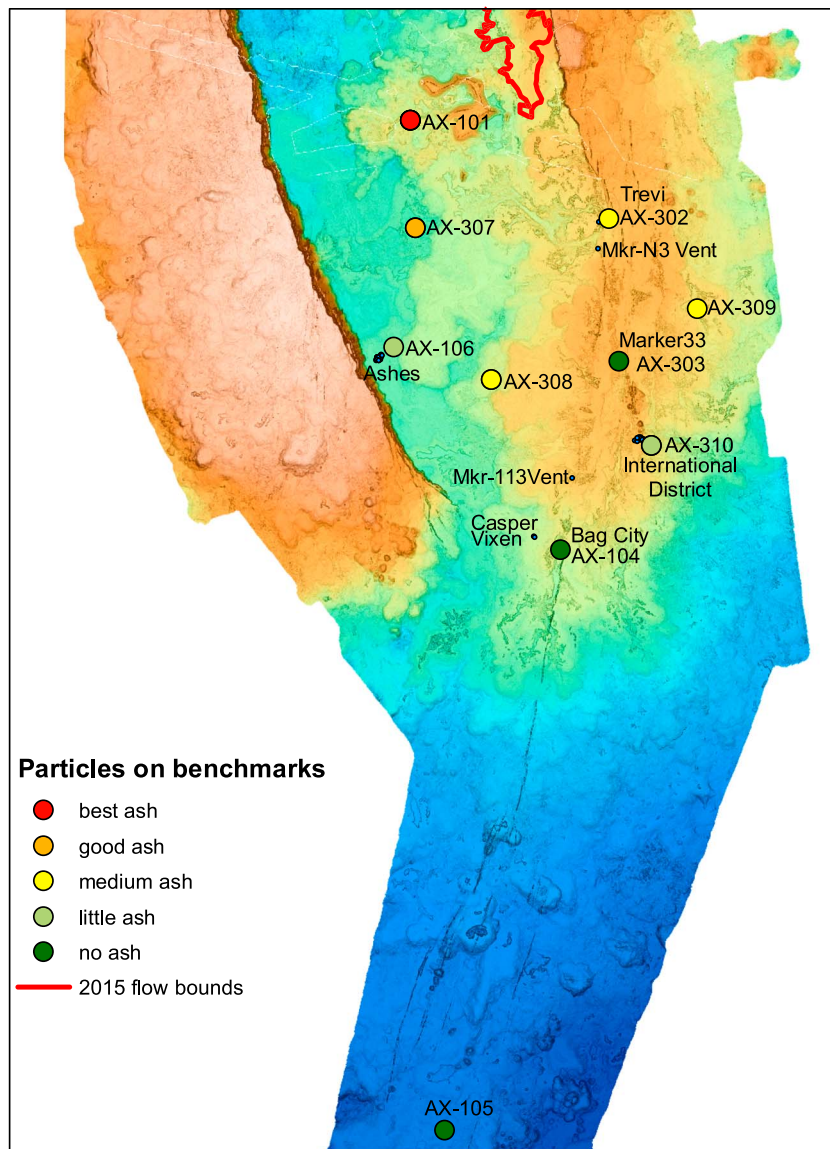
Figure 5. Map of the summit of Axial Seamount showing the locations of benchmarks and a semiquantitative measure of the amount of pyroclastic glass shards deposited during the 2015 eruption.

~ 0.85, and $(La/Yb)_{C1}$ ~ 1.11. All 2011 lavas are similar in major and trace elements to Group 1 prehistorical Axial lavas (Dreyer et al., 2013; Table 1 and Figure 4) and to the 1998 lavas described above, with the exception that the 2011 distal hummocky flow samples have significantly lower MgO and higher incompatible trace element abundances than Group 1 lavas from the caldera and upper south rift (Dreyer et al., 2013).

The 2011 flows partly buried 13 mapped flows (Clague et al., 2013) plus parts of several prehistorical cones on the upper south rift zone. The 2011 flows also buried 58.9% by area of the 1998 flows, including the sites where 43 of the 93 samples were collected prior to the 2011 eruption.

4.3. The 2015 Eruption

In 2015, 10 discrete flows erupted from a sequence of en echelon fissures starting in the east central caldera and continuing onto the northeast rim of the caldera before two westward steps to the north rift
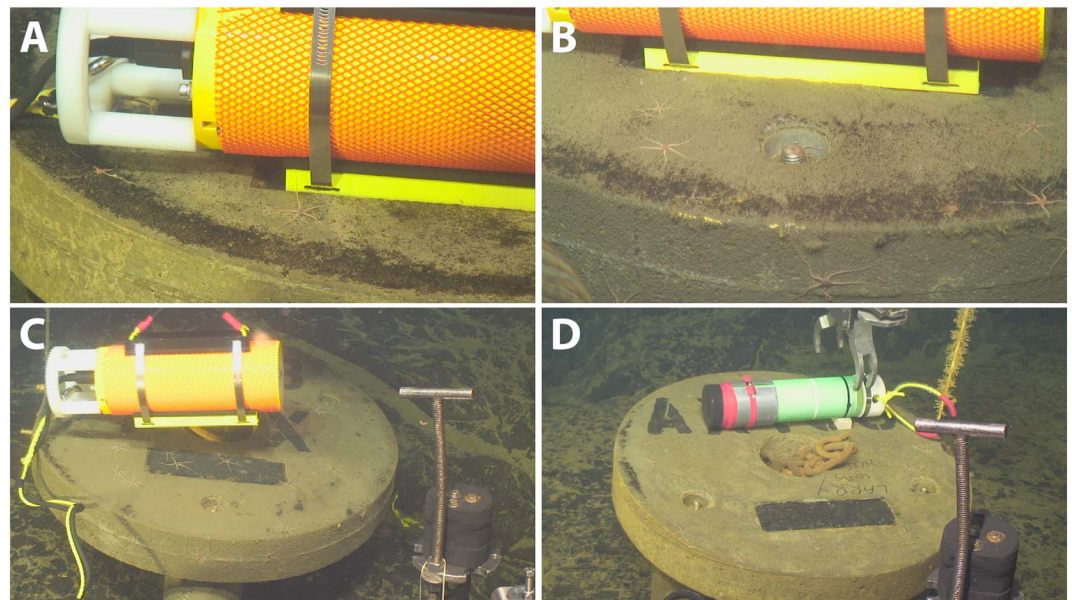
Figure 6. Video framegrabs from ROV *Jason* dive J2-823 showing 2015 ash on seafloor benchmarks, with varying amounts from most to least. (a) thickest ash at benchmark AX101 at the center of the caldera. (b) Medium-high ash at benchmarks AX307 located about 1 km south of AX101. (c) Medium ash at benchmark AX308. (d) Little ash at benchmark AX106.

zone (W. W. Chadwick et al., 2016; Clague et al., 2017; Figure 2d). The fissures total about 21 km in length. These lavas are more compositionally variable than those erupted in 1998 or 2011, with a range from 7.05 to 8.31 wt % MgO (Table 1 and Figure 3c). The 2015 lavas have a strong trend of decreasing MgO with increasing distance from the caldera, as shown by W. W. Chadwick et al. (2016) based on a subset of about half of the data used here. That pattern does not change with the additional data presented. The near-fissure lavas on the caldera floor (fissure A) have 8.03 to 8.31 wt % MgO (average 8.06 ± 0.19 wt % MgO) and contain 1–5% plagioclase phenocrysts up to ~3 mm in size. Near-fissure samples from the NE flank of the caldera (erupted from fissure B) have 7.83 to 8.03 wt % MgO (average 7.93 ± 0.08 wt % MgO). Glass from the single lava sample collected from fissure C contains 7.50 wt % MgO and more closely resembles the samples erupted from the north rift fissures D to G. Lavas erupted from fissures D to G (south to north) on the north rift have 7.05 to 7.66 wt % MgO, and MgO broadly decreases, with large ranges, from ~7.5 to ~7.2 wt % between 5.5 and 21 km from the southern end of the fissure system (Figure 3c). The group average is 7.56 ± 0.62 wt % MgO (2σ), only slightly higher than the caldera/upper rift samples from the 2011 and 1998 flows. The lavas erupted in the caldera and on the NE rim of the caldera are significantly more MgO-rich than any lava erupted in 2011, 1998, or during the preceding ~365 years when 19 prehistorical caldera lava flows were uniformly aphyric and had glass with 7.26–7.71% MgO (Clague et al., 2013). The higher MgO glass contents of the 2015 sparsely plagioclase-phyric caldera lavas are similar to those of plagioclase phyric and ultraphyric Group 2 lavas erupted between 650 and 730 years ago (Table 1) making this portion of the 2015 eruption the most MgO-rich melts erupted in the last six centuries at Axial Seamount.

Glasses erupted as pyroclastic shards in 2015 and sedimented out of the water column were also recovered from the top of a benchmark located near the center of the caldera (W. W. Chadwick et al., 2016; Table S1). The sample includes aphyric (MgO from 7.93 to 8.16 wt %) and microphyric shards (MgO from 7.59 to 7.97 wt %), and nearly encompass the compositional range observed in lava flow samples from fissures A on the caldera floor with 7.71 to 8.31 wt % MgO (for aphyric shards) and fissure B on the northeast caldera flank with 7.68 to 8.04 wt % MgO (for microphyric shards). A visual estimate of the amount of glass shards on all benchmarks in and near the caldera shows the greatest abundance at benchmark AX101 in the caldera center (Figures 5 and 6). The amount of ash on the other benchmarks decreased with distance from the 2015 eruptive vents; the most distal ones had none (Figure 5).

Lavas erupted closest to the caldera rim contain the greatest amount (~5%) of plagioclase phenocrysts up to 3 mm in length, but most of the rest of the 2015 lavas have ≪1% phenocrysts. More distal samples on the north rift with MgO < 7.35 wt % contain 1–4% small clusters of plagioclase plus clinopyroxene microlites, whereas samples nearer to but outside of the caldera have <1% microlites. All the lavas have slightly enriched incompatible element ratios (K_2O/TiO_2 = 0.116 ± 0.005, Zr/Nb ~ 19.5, Zr/Y ~ 3.13, $(La/Sm)_{C1}$ ~ 0.87, and $(La/Yb)_{C1}$ ~ 1.12; Table 1 and Figure 4) typical of Group 1 T-MORB.

The 2015 lava flows in the caldera partly buried 10 flows (Clague et al., 2013) and 46.5% of flow Ne. Much of the area on the northeast flank of the caldera and on the north rift were not mapped prior to the 2015 eruption, but several of the 2015 flows on the north rift buried sites sampled during remotely operated vehicle ROPOS dives R497 and R467 (J. Chadwick et al., 2005). Within the caldera, the southernmost part of the 2015 flows approached to within 100 m of the northernmost part of the 1998 flows.

5. Discussion

5.1. Are 2015 Lavas Representative of Group 1 or Group 2 Lavas?

Rhodes et al. (1990), J. Chadwick et al. (2005, 2014), and Dreyer et al. (2013) have described the origin of Axial Seamount lavas as MORB generated from mantle having a slight incompatible element enrichment derived from the Cobb hot spot. Dreyer et al. (2013), in particular, noted the range of compositions from N-MORB to T-MORB and showed that the two groups were generally erupted during different time periods. Despite the similarities of 2015 caldera glasses in MgO content and presence of plagioclase phenocrysts to Axial Seamount Group 2 N-MORB lavas (Dreyer et al., 2013), all 2015 samples are Group 1 T-MORB. There are no significant differences in any diagnostic trace element ratios (Table 1) or incompatible element patterns (Figure 4) between the higher-MgO samples from fissures 15A and 15B and the lower-MgO samples from the 2015 north rift zone fissures, or to 1998, 2011, or prehistorical lavas erupted in the past 365 years. This implies a nearly constant parent melt composition being supplied to the Axial magma system over that time period.

The higher than usual MgO contents in the fissure 15A and 15B samples (i.e., implying hotter eruption temperatures) is most likely linked to the short interval between the 2011 and 2015 eruptions, whereby mixing between recharge magma and resident magma and/or cooling and crystallization in the magma reservoir was inhibited. The rate of inflation observed between 2011 and 2015 was 4 times higher than before 2011, suggesting a higher magma supply rate (Nooner & Chadwick, 2016). This relatively hot recharge magma ascended to the surface near the southern end of the 2015 fissures, near the locations of the earliest earthquakes (Wilcock et al., 2016), center of deformation (Nooner & Chadwick, 2016), and most CO_2 supersaturated lavas (Jones et al., 2018). Rapid ascent, as suggested by the degree of CO_2 supersaturation of these lavas (Jones et al., 2018), may have aided in the entrainment of (mainly) plagioclase phenocrysts, perhaps from the roof of the reservoir. Degassing formed pyroclasts that deposited on a number of the benchmarks in and near the caldera (W. W. Chadwick et al., 2016; Figure 5). The appearance at the summit early in the eruption of the hottest, most gas-rich magma to erupt in 2015 is consistent with hot recharge magma having risen through resident more fractionated and degassed reservoir magma. The recharge magma could pond at the top of the reservoir and cool, degas, and mix with resident reservoir magma given adequate time. In 2015, the repose period was likely too short to allow mixing to blend the recharge magma with the resident magma.

In summary, all three historical lava flows have the slightly enriched chemical characteristics of Group 1 lavas, but the 2015 flows in the summit caldera and on the NE flank of the caldera have higher MgO content than any lava flow erupted in the past 365 years and also are plagioclase phyric rather than aphyric. We suggest that the more rapid ascent of these hottest 2015 lavas, while sharing the same compositional source as the lavas erupted 1998 and 2011, led to the entrainment or preservation of plagioclase phenocrysts, previously only found in Group 2 lava. The Group 2 lavas also have similarly elevated MgO contents as the early 2015 lavas but have distinct trace element compositions.

5.2. Compositional Variations During Each Eruption Along the Fissures

All three historical eruptions, as well as prehistorical flows (J. Chadwick et al., 2005), show decreases in MgO content of the glass, and therefore of eruption temperature, with distance from the caldera (Figure 3). We interpret these decreases in eruptive temperature as being caused by conductive cooling and

crystallization during magma transport in the dikes that propagate laterally away from the caldera and cross-cut cooler wall rocks (e.g., A. M. Rubin, 1993).

As a result of the added uncertainties introduced due to analyses on three different microprobes, the trend for the 1998 lava flows (Figure 3a) is not as clear along the 11 km of eruptive fissures as it is for the later 2011 (Figure 3b) and 2015 (Figure 3c) lava flows over longer fissures. Nonetheless, the data (especially the UC Davis and USGS in Menlo Park data) can be interpreted as showing a small decrease in MgO away from the caldera and the general trend is equivalent to a decrease in eruption temperature from 1185 to 1180 °C (Table S1), or a decrease in eruptive temperature of ~0.50 °C/km of fissure. The glass compositions fall along a calculated liquid line of descent for slightly less than 80% residual melts after crystallization of olivine, plagioclase, and less clinopyroxene from parental melts that have about 8.7% MgO (see Figure 3 in Dreyer et al., 2013). These 8.7% MgO parental melts could themselves be roughly 80% residual melts after crystallization of olivine plus plagioclase from near-primary melts with 9.7–9.8% MgO, similar to the most MgO-rich melts sampled from Axial Seamount (J. Chadwick et al., 2005; Portner et al., 2015).

The caldera and upper south rift 2011 lavas also show a small decrease in MgO away from the caldera from ~7.5 to ~7.2 wt % that corresponds to a decrease in eruption temperature of ~6 °C from ~1186 to ~1180 °C over ~10 km of fissure, or ~0.60 °C/km. The hummocky flow on the distal south rift has an average MgO content of 6.73 ± 0.12 wt % that indicates an average eruption temperature of 1171 ± 2 °C, or 15 °C cooler than the average of lavas ~31.5 km uprift at the north end of the fissure system. The temperature decreased along the entire dike/fissure at a rate of ~0.48 °C/km. If one considers only the gap between 20 and 31.5 km, MgO decreased from 7.2 to 6.73 wt %, equivalent to a decrease in temperature from ~1180 to ~1170 °C, or 0.87 °C/km, in which case the cooling rate of the dike appears to have increased as the dike reached the distal end of the rift zone. Alternatively, the variations observed in each eruption could be caused by variable mixing of caldera magma with magma stored in the rift. However, the most distal lavas in the 2011 and 2015 eruptions do not entrain plagioclase, olivine, and clinopyroxene phenocrysts of microphenocrysts one might expect to be present in evolved magmas stored in the rift.

Like the 1998 melts, 2011 glass compositions fall along a calculated liquid line of descent for slightly less than 80% residual melts after crystallization of olivine, plagioclase, and less clinopyroxene from parental melts that have about 8.7% MgO (see Figure 3 in Dreyer et al., 2013). These 8.7% MgO parental melts are themselves roughly 80% residual melts after crystallization of olivine plus plagioclase from estimated near-primary melts. The lower rift melt compositions also fall along calculated liquid line of descent (see Figure 3 in Dreyer et al., 2013) and crystallized about 15–20% more olivine, plagioclase, and clinopyroxene than the upper rift and near-caldera melts. Incompatible trace element concentrations for Nb, La, Ta, Hf, and Th increase by 15–21% during this modeled crystallization.

The 2015 caldera samples from near the eruptive fissures A–C have a steep decrease in MgO from ~8.3 to ~7.85 wt % along just 4.5 km of fissure, equivalent to a temperature decrease from ~1201 to ~1192 °C or 2 °C/km of fissure. Fissures C–G lavas broadly decrease in MgO from ~7.5 to ~7.2 wt % or in temperature from ~1186 to ~1180 °C along 15.5 km of fissure or 0.37 °C/km of fissure. There is a temperature gap of ~6 °C between lavas on the fissure on the northeast flank of the caldera to those on the north rift. Overall, MgO decreases from an average of ~8.3 to ~7.2 wt % over 21 km of fissure, equivalent to a ~21 °C decrease or 1 °C/km of fissure away from the caldera; most of the decrease occurs along the fissures in the caldera and on the NE flank of the caldera. The 2015 lavas have a much wider range in composition (~0.4 wt % MgO) and temperature (~7.5 °C) at any given distance along the north rift zone. This wide variation in eruptive temperature may reflect a less homogeneous mixture of recharge and resident magmas in the reservoir during the 2015 eruption.

Like the 1998 and 2011 lavas, the variations in the 2015 glasses also fall along liquid line of descent (see Figure 3 in Dreyer et al., 2013) and formed from ~22% crystallization of olivine, plagioclase, and clinopyroxene between the least and most-MgO rich melts. Incompatible trace element concentrations of La, Nb, Ta, Hf, and Th increase by 6–11% from average fissure 15A to average fissure 15E to 15J (Table 3). The most MgO-rich melts from within the caldera had previously crystallized ~30% olivine and plagioclase from estimated near-primary magmas. The more evolved lavas from the north rift lack plagioclase phenocrysts present in the lavas erupted on the caldera floor, but the glasses have common microlites of plagioclase, olivine, and clinopyroxene.

In summary, lavas transported in the feeder dikes down either the north or south rift zones cool at rates of 0.5–0.6 °C/km with rates of almost 0.9 °C/km for dikes that reach the deeper rift zones. This increase in cooling rates could be caused by cooler wall rocks or slower dike propagation downrift as driving pressure decreases during summit deflation. In contrast, lavas transported in dikes mainly under the northeast flank of the caldera cool at ~2 °C/km, or roughly 3–4 times more quickly. This difference in dike cooling rates appears to be correlated with the frequency of recent diking and eruption in the two settings. Frequent diking on the rift zones maintain hot wall rocks and low dike cooling rates. The upper south rift has had numerous young eruptions prior to 1998 and then just 13 years between 1998 and 2011 eruptions. Even the lower south rift 2011 hummocky flow on the distal south rift zone roughly followed the path of dike intrusion that took place in 1998, as evidenced from earthquake epicenters (Dziak & Fox, 1999). In contrast, high dike cooling rates characterize the eastern caldera floor where the last eruption (of flow Ne) took place 365 years ago or the northeast flank of the caldera where the last eruption (of flow Eg) took place 675 years ago (Clague et al., 2013) and wall rocks are colder. Eruption age constraints are few along the north rift. Near the caldera, flows are covered by a thick sequence of clastic deposits that date to at least 800 years ago, but the 2015 flows on the north rift start beyond those deposits where most flows have thin sediment cover that suggests they are probably more recent than 1650 CE. An alternative explanation to the rapid apparent cooling rates across the caldera floor and northeast flank of the caldera is that the variation in MgO content and calculated temperatures in lavas reflects compositional zoning or magma mixing in the shallow magma reservoir that underlies these areas (Arnulf et al., 2014, 2018; W. W. Chadwick et al., 2016).

5.3. Compositional Variations Within Flows Away From Fissures

We classified the samples from all three historical flows into groups collected proximal to the eruptive fissures (<200 m), distal from the fissures (>500 m), and in between (Table S1 and Figure 3). Only some of the more distal samples stand out as having lower MgO (Figure 2). All three flows are all surface flows with no evidence of having developed tube systems. The southernmost channelized flow erupted in 1998 from the south rift zone decreased in MgO by ~0.2 wt % (just larger than the estimated 2σ analytical uncertainty), so temperature may have decreased by ~3.8 °C as the lobe advanced downslope to the east for ~1.14 km, resulting in a cooling rate of ~3.3 °C/km. Several lobes of the 2011 flows advanced downslope as far as 3.4 km but show no systematic compositional changes and therefore no temperature gradients along the flow lobes.

Several 2015 flow lobes have enough samples collected away from the fissures to assess changes downflow. Flow 15A (caldera floor) has 8.06 ± 0.31 wt % MgO near fissure, 7.93% at middistances and 7.78% for the most distal samples and so ~0.28 wt % MgO (~5.5 °C) decrease along the 3.5 km flow or 1.5 °C/km as the flow advanced on the surface. Flow 15B on the northeast flank of the caldera has 7.93% near-fissure, 7.78% for middistance samples, and 7.76% for distal samples, and so MgO decreased 0.17 wt % (~3.2 °C cooling) during ~2.1 km of flow (or 1.5 °C/km).

The 1998 flow on the south rift (W. W. Chadwick et al., 2013; Clague et al., 2017) with the highest cooling rate flowed down a steep slope, so the flow may have been more turbulent and therefore cooled more rapidly than the 2015 flow lobes which advanced on less steep slopes. Only two other 2015 flow lobes (15E and 15H) sampled at mid-distance or distally are within the compositional range of the near-fissure samples. The apparent cooling rates for 1998 and 2015 flow lobes are ~2.5 to 4 times as rapid as observed for tube-fed flows during the Pu'u 'O'o eruption at Kilauea volcano, Hawaii (Helz et al., 2003). Comparable rates cannot be determined for the 2005–2006 EPR flows (Goss et al., 2010) because the lava compositions do not vary systematically away from the fissure. The apparent lack of a temperature gradient in the 2011 flow lobes suggests more complex processes were operative—perhaps with decreasing eruption temperatures during the eruption balancing cooling of the advancing flows.

5.4. Flow Heterogeneity

Each of these flows have statistically significant compositional heterogeneity. Accurately characterizing this aspect of lava flows requires collection of numerous and spatially well distributed samples. The apparent changes in MgO (and temperature) along flow lines are generally just larger than the 2σ analytical uncertainties of the analyses, so cooling rate during flow on the seafloor is still poorly constrained; all appear to cool significantly faster than for subaerial tube-fed flows.

Flow heterogeneity combines the compositional variations along the fissures discussed in section 5.2 and the chemical variations during emplacement on the seafloor discussed in section 5.3. A homogeneity index (HI), first applied to subaerial flows on Mauna Loa volcano in Hawaii (Rhodes, 1983), was later used to examine the compositional variability of submarine flows by K. H. Rubin et al. (1998, 2001). K. H. Rubin et al.'s results, based on 10 submarine flows, showed that more voluminous flows were more heterogeneous than less voluminous flows and that HI also varied with spreading rate with flows erupted on faster spreading ridges being less heterogeneous. The heterogeneity of three historical Axial lava flows also increase with volume and is controlled by varying amounts of crystallization since the lavas from the three eruptions have common parental magma compositions. The 24.1×10^6 m^3 1998 flow (volumes from Clague et al., 2017) has HI of 1.06 to 1.22 for samples analyzed at each of the three laboratories and an average for all samples of 1.21. The 94×10^6 m^3 2011 flows have an overall HI of 1.78 and HI of 0.85, 1.43, and 1.18 for flows from fissures A–E, F–H, and I, respectively. The 155.2×10^6 m^3 2015 flows have an overall HI of 2.10. However, only the 1998 flow plots close to the MORB correlation line of K. H. Rubin et al. (2001), with the two larger volume, more heterogeneous Axial Seamount flows having much lower HI than predicted from the correlation of HI to volume (K. H. Rubin et al., 2001, their Figure 2a) and much closer to the trend for more voluminous southern EPR flows. K. H. Rubin et al. (2001) speculated that some larger volume MORB flows might plot below the correlation and have lower HI than predicted because they underwent efficient mixing and/or have greater heat capacity, resulting in smaller differentiation gradients within the magma reservoir. The 2011 and 2015 Axial Seamount flows suggest that this is apparently the case. The 2005–2006 lava flows on the EPR have an HI of 1.57 (Goss et al., 2010) and an estimated volume of 22×10^6 m^3 (Soule et al., 2007), similar to other small volume MOR eruptions. Axial Seamount has a very similar spreading rate to the 1986 North Cleft pillow mounds, the pre-1986 North Cleft sheet flow, and the 1993 CoAxial pillow ridge (K. H. Rubin et al., 2001). At this roughly 60 mm/year spreading rate, the six flows from the JdFR have HIs that vary from a low of 1.21 for the 1998 Axial flow to 2.10 for the 2015 Axial flow and span much of the range in HI for all MORB flows with calculated HI (K. H. Rubin et al., 2001). Axial Seamount may not function in the same way as non–hot spot-influenced ridge segments, enabling eruptions with a wider range of volumes and HI. The Axial historical lava flows are heterogeneous in major elements, despite having the largest melt lens/reservoir on the MOR to date (Arnulf et al., 2014).

5.5. Origin of Glass Shards on Benchmark AX101

Clague et al. (2003, 2009) argued that glass shards, including fluidal and limu o Pele fragments, along the Gorda-JdFR system formed during strombolian eruptive activity. Helo et al. (2011) and Portner et al. (2015) describe glass shards with similar morphologies in thick deposits on the rim of Axial Seamount, and Sohn et al. (2008) described similar deposits from the Gakkel Ridge. Strombolian activity is most likely driven by accumulation of vesicles in rising magmas to form larger bubbles that burst through the lava surface at eruptive vents, as modeled by Head and Wilson (2003) and observed at West Mata Volcano (Resing et al., 2011). The shards were deposited on benchmark AX101 (the southernmost sample in Figure 2d; W. W. Chadwick et al., 2016; Nooner & Chadwick, 2016) after summer 2013 and sampled in summer 2015, only months after the 2015 eruption. The ash compositions are similar to those of lava flows erupted from fissures 15A and 15B with the aphyric shards most similar to fissure 15A lavas and the shards with microlites most similar to fissure 15B lavas. The 19 analyzed pyroclasts have an HI of 1.28 compared with an HI of 2.10 for all 2015 lavas, showing that they do not represent the full range of the erupted products in 2015. The absence of the lower MgO compositions among the pyroclasts may indicate that only fissures 15A and 15B (with an HI of 1.31) were characterized by pyroclastic activity, in addition to the effusive emplacement of flows, or that fissures 15C–L were simply farther away and the pyroclasts were not transported to the central caldera. Regardless, the pyroclasts erupted at fissure 15B were carried between 3.8 and 4.9 km to the SSW before settling on monument AX101 in the central caldera and at least 4.3 km to the SSE from fissure 15A to benchmark AX310 (Figure 5), consistent with the mapped >5 km dispersal of glass shards in the Escanaba Trough from the prehistorical northern Escanaba (NESCA) eruption in the Escanaba Trough (Clague et al., 2009).

5.6. The Utility of Prompt Mapping and Sampling of New Flows

The detailed mapping and sampling of lava flows at Axial Seamount represents the most complete and extensive effort at an active submarine volcano. Our experiences and results point out some of the

benefits of these types of studies but also some of the complexities and challenges in deciphering MOR-related magmatic events/histories. With three eruptions occurring in the span of just 17 years, it is important that posteruptive lava mapping and sampling takes place within a relatively short time, before flows are potentially buried by subsequent eruptions. Fortunately, much of the summit of Axial Seamount was mapped with high-resolution AUV bathymetry before and after the emplacement of the 2011 and 2015 flows, and depth differences clearly map out the extent of the new flows, particularly where the flow margins are thick (Caress et al., 2012; W. W. Chadwick et al., 2016; Clague et al., 2017). With AUV mapping now completed (Figure 1) of the entire summit, the north rift beyond the extent of the 2015 flows, and most of the south rift zone (see Figure 1 in Clague et al., 2017), repeat mapping will define the flows from future eruptions.

Channelized flows, such as most flows in and near the caldera on Axial Seamount or along the fast-spreading EPR (e.g., Bergmanis et al., 2007; Soule et al., 2007), require high-resolution repeat AUV mapping, because they are generally too thin to be detected by ship-based bathymetric resurveys which are at lower resolution. Channelized flows also tend to bury much larger areas than the thicker hummocky flows common farther down the rift zones. Assessing the distribution and origins of pyroclastic glass shards produced during future eruptions will be aided by deployment of closable containers in the caldera, on caldera rims, and on the rift zones, as well as the numerous benchmarks used to make pressure measurements (Nooner & Chadwick, 2016) that are mainly located inside the caldera and on the upper south rift.

5.7. Rift Zones and Seafloor Spreading

At Axial Seamount, the locations of the eruptive fissures do not define a narrow band where seafloor spreading occurs but instead jump back and forth over a zone at least 600–700 m wide. The fissures for the 2015 flows in the eastern caldera near the southern end are located ~260 m west of the 1998 fissures and ~400 m west of the 2011 fissures. Farther north on the east northeast flank of the caldera, the 2015 fissures are located ~300 m east of the flow Ne fissures and ~200–220 m west of the flow Sg fissures mapped by Clague et al. (2013). The 1998 and 2011 south rift fissures are generally very close to or even coincide with locations of previous eruptive fissures as described in Caress et al. (2012) and W. W. Chadwick et al. (2013). A similarly wide extension zone was shown to occur at the Endeavor segment of JdFR (Clague et al., 2014).

5.8. Eruptive and Intrusive Volumes Compared With Magma Reservoir Volumes

The percent of the subcaldera reservoir volume that erupted as lava flows was only 0.25–0.6% in 2015, 0.16–0.36% in 2011, and 0.04–0.09% in 1998, assuming that the volume of melt estimated to reside in the reservoir (26–60 km^3) has not changed since the multichannel seismic experiment (Arnulf et al., 2018) was conducted in 2002. If estimated volumes of the dikes intruded down the rift zones are included, then the percent of the volume of the magma reservoir that intruded and erupted might have reached 0.5–1.2% (in 2015) and slightly less in 2011 and 1998, estimated using a 2-km-tall dike (approximate thickness of ocean crust layer 2B; e.g., McLain, 2003) that is 2 m thick (observed open fissure widths) and 50, 35, and 24 km long in 1998, 2011, and 2015, respectively (measured in GIS). These estimates are similar to those of Arnulf et al. (2018) that <1% of the stored melt was intruded or erupted during the historical eruptions. These estimates are far smaller than the estimated 15% of the volume of the axial magma lens estimated for the 2005–2006 eruption on the EPR at 9°N (Soule et al., 2007), although the difference may reflect the enhanced flux from the Cobb hot spot on the magma storage reservoir at Axial Seamount (J. Chadwick et al., 2014).

Recharge of the reservoir (e.g., Nooner & Chadwick, 2016) took place in 4,834 days between the start of the 1998 and the start of the 2011 eruption but in just 1,478 days between the start of the 2011 and the start of the 2015 eruption. The recharge period prior to the 1998 eruption is >13 years and probably <20–25 years after the eruption of the Bag City lava flow (flow Sb in Clague et al., 2013) as it predates a sidescan survey done in 1985 (W. W. Chadwick et al., 2013) and is consistent with the average recurrence interval of 15 ± 4 years for the last 24 eruptions inside the caldera (Clague et al., 2013) This range suggests that the recharge period prior to 1998 was at least as long as the 4,834 days between the 1998 and 2011 eruptions. Post-2015 inflation rates suggest that the recharge period following the 2015 eruption may be closer to that from 2011 to 2015 than to the 1998 to 2011 recharge period.

6. Conclusions

(1) The glass compositions for the historical eruptions at Axial Seamount in 1998, 2011, and 2015 each show increasing amounts of differentiation with distance from the caldera, as measured by decreasing MgO content and calculated temperatures.

(2) Eruption temperatures decrease along the upper rift zones at ~0.5–0.6 °C/km and are attributed to cooling of the dikes against cooler wallrocks during lateral propagation. The rate of cooling increases to ~0.9 °C/km in the distal south rift during the 2011 eruption, probably because the wallrocks are cooler since they have less frequent dike intrusions and/or because of decreasing dike propagation rate with time.

(3) The initial phase of the 2015 eruption, on the eastern caldera floor and northeast rim of the caldera, erupted the hottest magma, at ~1200 °C, and the most phyric magma (up to ~5% crystals) erupted near the summit of Axial Seamount in the past 370 years and perhaps as long as 715 years.

(4) Despite the higher magma eruption temperatures and higher crystal content of the summit 2015 lavas (characteristic of Group 2 normal-MORB lavas erupted between 715 and 800 years ago), all lavas from the three historical eruptions are Group 1 transitional-MORB. The hotter summit 2015 eruption temperatures apparently were caused by a shorter than normal repose period and higher magma supply rate following the 2011 eruption.

(5) The shorter repose period also resulted in eruption of gas-rich magma at the summit in 2015 and strombolian eruptive activity that produced abundant pyroclasts that were transported 3.8–4.9 km to the SSW from fissure B before settling in the center of the caldera. The more rapid rise rate of these initial gas-rich magmas carried phenocrysts of plagioclase and lesser olivine to the surface from the magma reservoir.

References

Arnulf, A. F., Harding, A. J., Kent, G. M., Carbotte, S. M., Canales, J. P., & Nedimovic, M. R. (2014). Anatomy of an active submarine volcano. *Geology*, *42*(8), 655–658. https://doi.org/10.1130/G35629.1

Arnulf, A. F., Harding, A. J., Kent, G. M., & Wilcock, W. S. D. (2018). Structure, seismicity and accretionary processes at the hotspot-influenced Axial Seamount on the Juan de Fuca Ridge. *Journal of Geophysical Research: Solid Earth*, *123*, 4618–4646. https://doi.org/10.1029/2017JB015131

Baker, E. T., Chadwick, W. W. Jr., Cowen, J. P., Dziak, R. P., Rubin, K. H., & Fornari, D. J. (2012). Hydrothermal discharge during submarine eruptions: The importance of detection, response, and new technology. *Oceanography*, *25*(1), 128–141. https://doi.org/10.5670/oceanog.2012.11

Bergmanis, E. C., Sinton, J., & Rubin, K. H. (2007). Recent eruptive history and magma reservoir dynamics on the southern East Pacific Rise at 17°39′S. *Geochemistry, Geophysics, Geosystems*, *8*(12), Q12O06. https://doi.org/10.1029/2007GC001742

Caress, D. W., Clague, D. A., Paduan, J. B., Martin, J. F., Dreyer, B. M., Chadwick, W. W. Jr., et al. (2012). Repeat bathymetric surveys at 1-metre resolution of lava flows erupted at Axial Seamount in April 2011. *Nature Geoscience*, *5*(7), 483–488. https://doi.org/10.1038/ngeo1496

Chadwick, J., Keller, R., Kamenov, G., Yogodzinski, G., & Lupton, J. (2014). The Cobb hot spot: HIMU-DMM mixing and melting controlled by a progressively thinning lithospheric lid. *Geochemistry, Geophysics, Geosystems*, *15*, 3107–3122. https://doi.org/10.1002/2014GC005334

Chadwick, J., Perfit, M., Ridley, I., Jonasson, I., Kamenov, G., Chadwick, W., et al. (2005). Magmatic effects of the Cobb hot spot on the Juan de Fuca Ridge. *Journal of Geophysical Research*, *110*, B03101. https://doi.org/10.1029/2003JB002767

Chadwick, W. W. Jr., Clague, D. A., Embley, R. W., Perfit, M. R., Butterfield, D. A., Caress, D. W., et al. (2013). The 1998 eruption at Axial Seamount: New insights on submarine lava flow emplacement from high-resolution mapping. *Geochemistry, Geophysics, Geosystems*, *14*, 3939–3968. https://doi.org/10.1002/ggge.20202

Chadwick, W. W. Jr., Paduan, J. B., Clague, D. A., Dreyer, B. M., Merle, S. G., Bobbitt, A. M., et al. (2016). Voluminous eruption from a zoned magma body after and increases in supply rate at Axial Seamount. *Geophysical Research Letters*, *43*, 12,063–12,070. https://doi.org/10.1002/2016GL071327

Clague, D. A., Davis, A. S., & Dixon, J. E. (2003). Submarine strombolian eruptions along the Gorda mid-ocean ridge. In J. D. L. White, J. L. Smellie, & D. A. Clague (Eds.), *Explosive subaequeous volcanism, American Geophysical Union Monograph* (Vol. 140, pp. 11–128).

Clague, D. A., Dreyer, B. M., Paduan, J. B., Martin, J. F., Caress, D. W., Gill, J. B., et al. (2014). Eruptive and tectonic history of the Endeavour segment of the Juan de Fuca Ridge based on AUV mapping and lava flow ages. *Geochemistry, Geophysics, Geosystems*, *15*, 3364–3391. https://doi.org/10.1002/2014GC005415

Clague, D. A., Dreyer, B. M., Paduan, J. B., Martin, J. F., Chadwick, W. W. Jr., Caress, D. W., et al. (2013). Geologic history of the summit of Axial Seamount, Juan de Fuca Ridge. *Geochemistry, Geophysics, Geosystems*, *14*, 4403–4443. https://doi.org/10.1002/ggge.20240

Clague, D. A., Paduan, J. B., Caress, D. W., Chadwick, W. W. Jr., Le Saout, M., Dreyer, B., & Portner, R. A. (2017). High-resolution AUV mapping and targeted ROV observations of three historical lava flows at Axial Seamount. *Oceanography*, *30*(4), 82–99. https://doi.org/10.5670/oceanog.2017.426

Clague, D. A., Paduan, J. B., & Davis, A. S. (2009). Widespread strombolian eruptions of mid-ocean ridge basalt. *Journal of Volcanology and Geothermal Research*, *180*(2–4), 171–188. https://doi.org/10.1016/j.jvolgeores.2008.08.007

Cowen, J. P., Baker, E. T., & Embley, R. W. (2004). Detection of and response to mid-ocean ridge magmatic events: Implications for the sub-surface biosphere. In W. S. D. Wilcock, et al. (Eds.), *The subseafloor biosphere at mid-ocean ridges* (pp. 227–243). Washington, DC: American Geophysical Union. https://doi.org/10.1029/144GM15

Desonie, D., & Duncan, R. (1990). The Cobb-Eickelberg seamount chain: Hotspot volcanism with a mid-ocean ridge basalt affinity. *Journal of Geophysical Research*, *95*(B8), 12,697–12,711. https://doi.org/10.1029/JB095iB08p12697

Dreyer, B. M., Clague, D. A., & Gill, J. B. (2013). Petrologic variability of recent magmatism at Axial Seamount summit, Juan de Fuca Ridge. *Geophysics, Geochemistry, Geosystems*, *14*, 4306–4333. https://doi.org/10.1002/ggge.20239

Dziak, R. P., Cowen, J., Baker, E. T., Bohnenstiehl, D., Chadwick, W. W. Jr., Resing, J. A., & Embley, R. W. (2006). Detecting volcanic events in the northeast Pacific. *Eos, Transactions American Geophysical Union*, *87*(4), 37, 42.

Dziak, R. P., & Fox, C. G. (1999). The January 1998 earthquake swarm at Axial Volcano, Juan de Fuca Ridge: Hydroacoustic evidence of seafloor volcanic activity. *Geophysical Research Letters*, *26*(23), 3429–3432. https://doi.org/10.1029/1999GL002332

Dziak, R. P., Hammond, S. R., & Fox, C. G. (2011). A 20-year hydroacoustic time series of seismic and volcanic events in the northeast Pacific Ocean. *Oceanography*, *24*(3), 280–293. https://doi.org/10.5670/oceanog.2011.79

Embley, R. W., Murphy, K. M., & Fox, C. G. (1990). High resolution studies of the summit of Axial volcano. *Journal of Geophysical Research*, *95*(B8), 12,785–12,812. https://doi.org/10.1029/JB095iB08p12785

Goss, A. R., Perfit, M. R., Ridley, W. I., Rubin, K. H., Kamenov, G. D., Soule, S. A., et al. (2010). Geochemistry of lavas from the 2005–2006 eruption at the East Pacific Rise, 9°46′N–9°56′N: Implications for ridge crest plumbing and decadal changes in magma chamber compositions. *Geochemistry, Geophysics, Geosystems*, *11*, Q05T09. https://doi.org/10.1029/2009GC002977

Head, J. W. III, & Wilson, L. (2003). Deep submarine pyroclastic eruptions: Theory and predicted landforms and deposits. *Journal of Volcanology and Geothermal Research*, *121*(3-4), 155–193. https://doi.org/10.1016/S0377-0273(02)00425-0

Helo, C., Longpre, M. A., Shimizu, N., Clague, D. A., & Stix, J. (2011). Explosive eruptions at mid-ocean ridges driven by CO_2-rich magmas. *Nature Geoscience*, *4*(4), 260–263. https://doi.org/10.1038/ngeo1104

Helz, R. T., Clague, D. A., Mastin, L. G., & Rose, T. R. (2014). Electron microprobe analyses of glasses from Kilauea tephra units, Kilauea volcano, Hawaii. U.S. Geological Survey Open File Report 2014-1090 (24 p.). https://doi.org/10.3133/ofr20141090

Helz, R. T., Heliker, C., Hon, K., & Mangan, M. (2003). Thermal efficiency of lava tubes in the Puu Oo eruption. In C. Heliker, D. A. Swanson, & T. J. Takahasji (Eds.), *The Puu Oo-Kupainaha eruption of Kilauea Volcano, Hawaii: The first 20 years*, U.S. Geological Survey Professional Paper (Vol. 1676, pp. 105–120).

Jarosewich, E., Nelan, J. A., & Norberg, J. A. (1980). Reference samples for electron microprobe analysis. *Geostandards Newsletter*, *4*(1), 43–47. https://doi.org/10.1111/j.1751-908X.1980.tb00273.x

Johnson, H. P., & Embley, R. W. (1990). Axial Seamount: An active ridge axis volcano on the central Juan de Fuca Ridge. *Journal of Geophysical Research*, *95*(B8), 12,689–12,696. https://doi.org/10.1029/JB095iB08p12689

Jones, M. R., Soule, S. A., Gonnermann, H., LeRoux, V., & Clague, D. A. (2018). Ascent and emplacement rates during the 2011 Axial Seamount eruption based on CO2 degassing. *Earth and Planetary Science Letters*, *494*, 32–41. https://doi.org/10.1016/j.epsl.2018.04.044

Langmuir, C. H., Klein, E. M., & Plank, T. (1992). Petrological systematics of mid-ocean ridge basalts: Constraints on melt generation beneath ocean ridges. In *Mantle flow and melt generation at mid-ocean ridges*, American Geophysical Union Monograph (Vol. 71, pp. 183–280).

McClain, J. S. (2003). Ophiolotes and the interpretation of marine geophysical data: How well does the ophiolite model work for the Pacidfic Ocean crust? In Y. Dilek & S. Newcomb (Eds.), *In ophiolite concept and the evolution of geological thought*, Geological Society of America Special Paper (Vol. 373, pp. 173–185).

Nooner, S. L., & Chadwick, W. W. Jr. (2016). Inflation-predictable behavior and co-eruption deformation at Axial Seamount. *Science*, *354*(6318), 1399–1403. https://doi.org/10.1126/science.aah4666

O'Neill, H. S. C., & Jenner, F. E. (2012). The global pattern of trace-element distributions in ocean floor basalts. *Nature*, *491*(7426), 698–704. https://doi.org/10.1038/nature11678

Perfit, M. R., & Chadwick, W. W. Jr. (1998). Magmatism at mid-ocean ridges: Constraints from volcanological and geochemical investigations. In W. R. Buck, P. T. Delaney, J. A. Karson, & Y. Lagabrielle (Eds.), *Faulting and magmatism at mid-ocean ridges*, Geophysical Monograph Series (Vol. 106, pp. 59–116). Washington, DC: American Geophysical Union.

Portner, R. A., Clague, D. A., Dreyer, B. D., Helo, C., Martin, J. F., & Paduan, J. B. (2015). Contrasting styles of deep-marine explosive eruptions revealed from Axial Seamount push core records. *Earth and Planetary Science Letters*, *423*, 219–231. https://doi.org/10.1016/j.epsl.2015.03.043

Resing, J. A., Embley, R., Rubin, K. H., Lupton, J., Baker, E., Baumberger, T., et al. (2011). Active submarine eruption of in the northeastern Lau Basin. *Nature Geoscience*, *4*(11), 799–806. https://doi.org/10.1038/ngeo1275

Rhodes, J. M. (1983). Homogeneity of lava flows: Chemical data for historic Mauna loan eruptions. *Journal of Geophysical Research*, *88A*, 869–879. https://doi.org/10.1029/JB088iS02p0A869

Rhodes, J. M., Morgan, C., & Liias, R. A. (1990). Geochemistry of Axial Seamount lavas: Magmatic relationship between the Cobb hotspot and the Juan de Fuca Ridge. *Journal of Geophysical Research*, *95*(B8), 12,713–12,733. https://doi.org/10.1029/JB095iB08p12713

Rubin, A. M. (1993). On the thermal viability of dikes leaving magma chambers. *Geophysical Research Letters*, *20*(4), 257–260. https://doi.org/10.1029/92GL02783

Rubin, K. H., Smith, M. C., Bergmanis, E. C., Perfit, M. R., Sinton, S. M., & Batiza, R. (2001). Geochemical heterogeneity within mid-ocean ridge lava flows: Insights into eruption, emplacement, and global variations in magma generation. *Earth and Planetary Science Letters*, *188*(3-4), 349–367. https://doi.org/10.1016/S0012-821X(01)00339-9

Rubin, K. H., Smith, M. C., Perfit, M. R., Christie, D. M., & Sacks, L. F. (1998). Geochronology and petrology of lavas from the 1996 north Gorda ridge eruption. *Deep Sea Research, Part II*, *45*(12), 2571–2597. https://doi.org/10.1016/S0967-0645(98)00084-8

Rubin, K. H., Soule, S. A., Chadwick, W. W. Jr., Fornari, D. J., Clague, D. A., Embley, R. W., et al. (2012). Volcanic eruptions in the deep sea. *Oceanography*, *25*(1), 142–157. https://doi.org/10.5670/oceanog.2012.12

Sinton, J., Bergmanis, E., Rubin, K., Batiza, R., Gregg, T. K. P., Gronvold, K., et al. (2002). Volcanic eruptions on mid-ocean ridges: New evidence from the superfast spreading East Pacific Rise, 17-19°S. *Journal of Geophysical Research*, *107*(B6), 2115. https://doi.org/10.1029/2000JB000090

Sohn, R. A., Willis, C., Humphris, S., Shank, T., Singh, H., Edmonds, H. N., et al. (2008). Explosive volcanism on the ultraslow-spreading Gakkel ridge, Arctic Ocean. *Nature*, *453*(7199), 1236–1238. https://doi.org/10.1038/nature07075

Soule, S. A., Fornari, D. J., Perfit, M. R., & Rubin, K. (2007). New insights into mid-ocean ridge volcanic processes from the 2005–2006 eruption of the East Pacific Rise, 9°46′N–9°56′N. *Geology*, *35*(12), 1079–1082. https://doi.org/10.1130/G23924A.1

Sugawara, T. (2000). Empirical relationships between temperature, pressure, and MgO content in olivine and pyroxene saturated liquid. *Journal of Geophysical Research*, *105*(B4), 8457–8472. https://doi.org/10.1029/2000JB900010

Sun, S.-S., & McDonough, W. F. (1989). Chemical and isotopic systematics of oceanic basalts: Implications for mantle composition and processes. In A. D. Saunders & M. J. Norry (Eds.), *Magmatism in the ocean basins*, Geological Society Special Publication (pp. 313–345).

West, M., Menke, W., Tolstoy, M., Webb, S., & Sohn, R. (2001). Magma storage beneath Axial volcano on the Juan de Fuca mid-ocean ridge. *Nature*, *25*, 833–837.

Wilcock, W. S. D., Dziak, R. P., Tolstoy, M., Chadwick, W. W. Jr., Nooner, S. L., Bohnenstiehl, D. R., et al. (2018). The recent volcanic history of Axial Seamount: Geophysical insights into past eruption dynamics with an eye toward enhanced observations of future eruptions. *Oceanography*, *31*(1), 114–123. https://doi.org/10.5670/oceanog.2018.117

Wilcock, W. S. D., Tolstoy, M., Waldhauser, F., Garcia, C., Tan, Y. J., Bohnenstiehl, D. R., et al. (2016). Seismic constraints on caldera dynamics from the 2015 Axial Seamount eruption. *Science*, *354*, 1395–1399. https://doi.org/10.1126/science.aah5563

Yeo, I. A., Clague, D. A., Martin, J. F., Paduan, J. B., & Caress, D. W. (2013). Pre-eruptive flow focussing in dikes feeding historical pillow ridges on the Juan de Fuca and Gorda ridges. *Geochemistry, Geophysics, Geosystems*, *14*, 3586–3599. https://doi.org/10.1002/ggge.20210